Compressive geoacoustic inversion using ambient noise

Caglar Yardim, Peter Gerstoft, William S. Hodgkiss, et al.

Citation: The Journal of the Acoustical Society of America **135**, 1245 (2014); doi: 10.1121/1.4864792
View online: https://doi.org/10.1121/1.4864792
View Table of Contents: https://asa.scitation.org/toc/jas/135/3
Published by the Acoustical Society of America

Compressive geoacoustic inversion using ambient noise

Caglar Yardim,[a] Peter Gerstoft, William S. Hodgkiss, and James Traer
Marine Physical Laboratory, Scripps Institution of Oceanography, La Jolla, California 92093-0238

(Received 30 September 2013; revised 13 January 2014; accepted 28 January 2014)

Surface generated ambient noise can be used to infer sediment properties. Here, a passive geoacoustic inversion method that uses noise recorded by a drifting vertical array is adopted. The array is steered using beamforming to compute the noise arriving at the array from various directions. This information is used in two different ways: Coherently (cross-correlation of upward/downward propagating noise using a minimum variance distortionless response fathometer), and incoherently (bottom loss vs frequency and angle using a conventional beamformer) to obtain the bottom properties. Compressive sensing is used to invert for the number of sediment layer interfaces and their depths using coherent passive fathometry. Then the incoherent bottom loss estimate is used to refine the sediment thickness, sound speed, density, and attenuation values. Compressive sensing fathometry enables automatic determination of the number of interfaces. It also tightens the sediment thickness priors for the incoherent bottom loss inversion which reduces the search space. The method is demonstrated on drifting array data collected during the Boundary 2003 experiment. © *2014 Acoustical Society of America*
[http://dx.doi.org/10.1121/1.4864792]

PACS number(s): 43.60.Pt, 43.30.Pc, 43.60.Fg [SED] Pages: 1245–1255

I. INTRODUCTION

Geoacoustic inversion estimates ocean environment parameters such as the water column sound speed profile (SSP) and seafloor parameters such as the sediment layer thicknesses, SSPs, density, and attenuation values. This paper introduces a passive geoacoustic inversion algorithm for use with drifting vertical line array (VLA) data. The sea-surface generated ambient noise observed by the VLA is used to invert for the sediment parameters. This inversion algorithm has two important features.

First, passive fathometry[1] and bottom loss measurements[2] are used together. Passive fathometry is a coherent technique that depends on the cross-correlation of upward and downward pointing beams and the bottom loss method is an incoherent technique that depends on the ratio of noise levels coming from different matched pairs of vertical arrival angles. Inversion methods that use either one of these have different properties and performance characteristics. Thus, using both of them together is an attractive combination. Here, the fathometer is used to estimate the water depth, the number of layers, and sediment thicknesses. This is followed by an inversion that uses incoherent bottom loss measurements, estimating the sound speed, attenuation, and density profiles in addition to refining the previously obtained sediment thickness values.

Second, compressive sensing (CS) is incorporated in the fathometer inversion. Here we take advantage of the sparse nature of sediment formations where there are a finite number of layer interfaces that create strong reflections. CS provides a theoretical framework that enables expressing the problem as a convex optimization problem which then can be solved efficiently.[3,4]

In recent years, CS has been used in diverse fields.[5–8] In addition to some early applications,[9] recent underwater acoustic work includes sensor network representations,[10] compressive channel sensing for underwater communication,[11,12] beamforming,[13] and matched-field processing.[14] Sparsely distributed reflector depths can be recovered using CS as long as a spatially sparse representation that can represent the fathometer output using linear functions exists.[15,16] CS achieves this by minimizing not only the error between the observation and the forward model but also the number of reflections.

Ocean acoustic passive fathometry is a coherent method that computes the cross-correlation between the upward and downward propagating noise.[1,17,18] A geoacoustic inversion algorithm based on passive fathometry then can be used to infer the sediment properties. This approach to fathometry is a passive method since it only uses the surface-generated noise field. It requires the decomposition of the ambient noise wave field into its upward and downward propagating components. A common way of achieving this is using beamforming to steer the VLA. Adaptive fathometry based on the minimum variance distortionless response (MVDR)[18–20] and the white noise constrained (WNC) beamformers[19] has been shown to outperform fathometry that uses conventional beamforming. This is due to the fact that the adaptive beamformers are able to suppress much better noise coming from unwanted angles. A multiple model particle filter is used in Ref. 21 to track the range-dependent sediment thicknesses in an environment where the number of interfaces changes. Here MVDR fathometry is used together with CS to estimate the water depth and sediment thicknesses.

Bottom loss estimation is another passive inversion method that uses ocean ambient noise.[2] This method is based on the ratio of the bottom-reflected upward propagating noise power to the downward propagating surface-generated noise power.[22,23] Since the method is based on the ratio of noise powers, it is an incoherent method. The sensitivity of this method to parameters such as array tilt, water absorption, and non-surface generated noise sources is studied in

[a]Author to whom correspondence should be addressed. Electronic mail: cyardim@ucsd.edu

Ref. 24. Genetic algorithms (GA),[23] Bayesian,[25] and trans-dimensional[26] algorithms have been applied to invert for the bottom properties.

Compressive sensing, coherent passive fathometer, and incoherent bottom loss calculations are summarized in Secs. II, III A, and III B, respectively. A geoacoustic inversion algorithm that utilizes all three is provided along with the application to drifting array data from the Boundary 2003 Experiment in Sec. IV.

II. COMPRESSIVE SENSING

Assume $\mathbf{b}$ is the data vector of N measurements (e.g., the passive fathometer output at various depths), and $\mathbf{x}$ is the vector of M unknown parameters (e.g., reflection coefficients of acoustic reflectors located at a dense vertical grid of M depths in the sediment), where $N<M$. As a linear system, the forward model can be represented by an $N\times M$ matrix $\mathbf{S}$:

$$\mathbf{b}=\mathbf{S}\mathbf{x}, \tag{1}$$

where the columns of $\mathbf{S}$ represents the reflection response wavelet for each reflector. Unfortunately, this is an underdetermined problem with infinite solutions. Regularization often is used with this type of problem by adding a second term to the cost function that penalizes undesirable solutions. This gives

$$\widehat{\mathbf{x}}=\underset{\mathrm{x}}{\operatorname{argmin}}\,\|\mathbf{x}\|_p \quad \text{subject to} \quad \mathbf{b}=\mathbf{S}\mathbf{x}, \tag{2}$$

where the desired optimal solution $\widehat{\mathbf{x}}$ is restricted to the $\mathbf{x}$ with minimum ℓ_p-norm. The most commonly used choice with $p=2$ seeks a solution with minimum vector length $||\mathbf{x}||_2$ in the parameter space.[7] The attractive feature of the ℓ_2-norm is that the inversion becomes convex with a unique solution. This can be calculated by recasting the problem using a Lagrange multiplier λ:

$$\widehat{\mathbf{x}}=\underset{\mathrm{x}}{\operatorname{argmin}}\,\|\mathbf{b}-\mathbf{S}\mathbf{x}\|_2+\lambda\|\mathbf{x}\|_2. \tag{3}$$

The optimal λ can be found by taking the derivative of the cost function relative to **x.** This results in the pseude-inverse solution:[7]

$$\widehat{\mathbf{x}}=\mathbf{S}^{\mathrm{H}}(\mathbf{S}\mathbf{S}^{\mathrm{H}})^{-1}\mathbf{b}. \tag{4}$$

There are many problems such as the geoacoustic inversion problem where $\mathbf{x}$ is sparse. For example, there are only a small number (K) of acoustic reflectors. Hence if $\mathbf{x}$ is the acoustic reflection strength at each depth, most of the entries of $\mathbf{x}$ are zero with only K non-zero entries with $K\ll N<M$. In this case, $\mathbf{x}$ is K-sparse.

Compressive sensing[3] is a technique that solves sparse inversion problems by taking advantage of the sparseness of the solution. When $\mathbf{x}$ is known to be sparse, the problem defined in Eq. (2) can be replaced with

$$\widehat{\mathbf{x}}=\underset{\mathrm{x}}{\operatorname{argmin}}\,\|\mathbf{x}\|_0 \quad \text{subject to}\|\mathbf{b}-\mathbf{S}\mathbf{x}\|_2\le\varepsilon. \tag{5}$$

The ℓ_0-norm $||\mathrm{x}||_0$ gives the number of non-zero entries in $\mathbf{x}$ so the optimal $\widehat{\mathbf{x}}$ is the sparsest of the possible solutions. This is a non-convex problem difficult to solve. Moreover the solution becomes unstable under noisy conditions.[27] Therefore, sparse recovery was not widely used until it was shown[3,15] that as long as a certain condition called the restricted isometry property (RIP) is met, the ℓ_0-norm can be replaced with the ℓ_1-norm:

$$\widehat{\mathbf{x}}=\underset{\mathrm{x}}{\operatorname{argmin}}\,\|\mathbf{x}\|_1 \quad \text{subject to}\|\mathbf{b}-\mathbf{S}\mathbf{x}\|_2\le\varepsilon. \tag{6}$$

Initially, matrices that are demonstrated to have RIP had random entries.[3] It later was demonstrated that ℓ_1-norm substitution also worked for numerous deterministic matrices,[28] as used here; see Eq. (16). Introducing the Lagrange multiplier λ one more time, the problem becomes

$$\widehat{\mathbf{x}}=\underset{\mathrm{x}}{\operatorname{argmin}}\,\|\mathbf{b}-\mathbf{S}\mathbf{x}\|_2+\lambda\|\mathbf{x}\|_1. \tag{7}$$

Unlike Eq. (5), Eq. (7) is a convex problem that can be solved efficiently with interior point solvers.[29] Selection of a good λ is critical for the CS inversion quality. λ enforces sparseness so the larger the value of λ, the more sparse the solution becomes and the convex optimization algorithm will give less weight to the ℓ_2 error norm.

III. AMBIENT NOISE PROCESSING

Ocean ambient noise is assumed to be generated at the sea surface by wave breaking and is modeled as a surface sheet of noise.[30] The surface generated noise can be measured by steering a VLA in the water column upwards toward the surface. At the same time, the noise travels down, interacts with the seafloor environment, and reflects back. The bottom- reflected noise can be measured by steering the VLA downwards. There are two basic ways of extracting information from noise observations about the geoacoustic environment, coherently (passive fathometry), and incoherently (bottom loss). Both methods incorporate the direct and bottom-reflected arrivals.

Noise-based inversion algorithms are strongly affected by the wind speed. If the ocean surface is too calm, there is not enough wave breaking that generates noise. If the noise level is too low, the inversion quality degrades. To a degree, low surface-generated noise levels are mitigated in both the coherent and incoherent methods by array gain during beamforming. An example of this is given for North of Elba Island, Italy[2] where the bottom loss cannot be extracted in calm conditions. Too much wind also is detrimental, especially when large ocean waves above the VLA alter the shape, tilt, and effective depth of the array and water column. Due to its coherent nature, the quality of passive fathometry results degrades faster than those of the bottom loss method with increasing sea state.[31]

A. Coherent processing: Passive fathometer

Passive fathometer data processing[1,17–19] is a coherent ambient noise processing technique that enables passive ocean bottom profiling. The fathometer output is the cross-correlation of downward traveling sea surface noise generated just above the VLA with the upward traveling reflection

of itself from the seabed, see Fig. 1(a). To achieve this, conventional or adaptive beamforming is used on the VLA data. Beamforming allows the array to look up and down while rejecting arrivals from other angles, particularly the higher level arrivals coming from around the horizontal direction (e.g., due to regional shipping activity). Adaptive beamforming such as MVDR and WNC beamforming[19] were used to improve the fathometer results.

Assume an equally-spaced VLA with L-elements where $l=0$ for the deepest hydrophone.[20] At each frequency, the acoustic pressure $\mathbf{p}$ across the array and the steering vector $\mathbf{w}$ are used to estimate the upward and downward propagating noise. This gives

$$\mathbf{w}_\theta = \frac{1}{L}\left[1\; e^{ikd\sin\theta} e^{2ikd\sin\theta}\cdots e^{i(L-1)kd\sin\theta}\right]^{\mathrm{T}}, \tag{8}$$

where d is the array element separation distance, $k=2\pi f/c_a$ is the wavenumber, c_a is the sound speed at the array location, θ is the steering angle with $\theta=0^\circ$ corresponding to broadside or horizontal propagation, and $^{\mathrm{T}}$ represents the transpose.

Using snapshots $\mathbf{p}_i$, $i=1,\ldots,N_p$, the data cross spectral density matrix $\mathbf{C}$ is estimated by averaging outer products of N_p snapshots, $\widehat{\mathbf{C}}=\sum_{i=1}^{N_p}\mathbf{p}_i\mathbf{p}_i^{\mathrm{H}}$.

Typically, noise coming from broadside angles is much stronger than that from the endfire directions.[18,19] Hence, horizontal noise can leak through the side lobes even when the array is steered up or down. Adaptive beamforming improves the fathometer results by suppressing the noise from unwanted directions. The MVDR fathometer output [Fig. 1(a)] is the cross-correlation between the upward and downward adaptively beamformed noise terms giving

$$\tilde{\mathbf{w}}_{-90} = \frac{\widehat{\mathbf{C}}^{-1}\mathbf{w}_{-90}}{\mathbf{w}_{-90}^{\mathrm{H}}\widehat{\mathbf{C}}^{-1}\mathbf{w}_{-90}}, \tag{9}$$

$$\tilde{\mathbf{w}}_{90} = \frac{\widehat{\mathbf{C}}^{-1}\mathbf{w}_{90}}{\mathrm{w}_{90}^{\mathrm{H}}\widehat{\mathbf{C}}^{-1}\mathbf{w}_{90}}, \quad \text{with} \quad \tilde{\mathbf{w}}_{90}\neq\tilde{\mathbf{w}}_{-90}^{*}, \tag{10}$$

$$B(f) = \tilde{\mathbf{w}}_{-90}^{\mathrm{H}}\widehat{\mathbf{C}}\tilde{\mathbf{w}}_{90}, \tag{11}$$

$$b(f) = \mathcal{F}^{-1}\{B(f)\}, \tag{12}$$

where $\tilde{\mathbf{w}}$ represents the MVDR weights. The time domain fathometer response is given by computing Eq. (11) for the frequencies inside the desired bandwidth and then calculating an inverse Fourier transform, see Eq. (12). If the layer sound speed values are known, the time delay information can be converted to reflector depths, $b(t)\rightarrow b(z)$. The time domain amplitudes of the peaks also relate to geoacoustic parameters.[17]

Assuming a step function transition at a layer interface, a simple frequency-independent reflection coefficient, and flat spectra for upward and downward propagating noise, and ignoring the multiple reflections between reflectors, each interface results in a $\mathrm{sinc}(\cdot)=\sin(\cdot)/(\cdot)$ function wavelet at the fathometer output corresponding to its two-way travel time (TWT).[18] Assuming a bandwidth W and effective sound speed c, the time-domain fathometer response at t caused by a reflector at a depth z_i (corresponding to TWT $t_i=2z_i/c$) is given by

$$b(\mathrm{t},z_i,A_i) = A_i\,\mathrm{sinc}\left(2W\left(t-\frac{2z_i}{c}\right)\right), \tag{13}$$

where A_i is the time-domain amplitude of the fathometer output. The fathometer output is available at sampling times corresponding to the acoustic data sampling frequency f_s. A bandwidth W of 3950 Hz is assumed throughout the paper.

Assuming K reflectors, the unknown parameter vector becomes $\mathbf{x}_{\mathrm{GA}}=[z_0\;A_0\;z_1\;A_1\cdots z_{K-1}\;A_{K-1}]^{\mathrm{T}}$ and the forward model for a fathometer inversion algorithm is given by

$$b(t,\mathrm{x}_{GA}) = \sum_{i=0}^{K-1} A_i\,\mathrm{sinc}\left(2W\left(t-\frac{2z_i}{c}\right)\right). \tag{14}$$

Note that the forward model is a nonlinear function of the geoacoustic parameter vector $\mathbf{x}_{\mathrm{GA}}$. This model can be used with GA (Ref. 23) or Bayesian type inversion algorithms.[21,25,26]

An alternative linear forward model can be constructed by defining an M-dimensional parameter vector $\mathbf{x}$ along a dense grid of depth values. Assume we discretize the depth with Δz spacing where each grid point is the depth of a potential reflector. A potential reflector at any of the M depths $\mathbf{z}=[z_0\;z_1\cdots z_{M-1}]^{\mathrm{T}}$ will generate a fathometer reflection amplitude A_i, $i=0,\ldots,M-1$. Defining the parameter vector as $\mathbf{x}=[A_0\,A_1\cdots A_{M-1}]^{\mathrm{T}}$, Eq. (14) can be rewritten as

$$\mathrm{b}(\mathrm{x}) = \mathbf{S}\mathrm{x} \tag{15}$$

$$= \begin{bmatrix} \mathrm{sinc}\left(2W\left(t_0-\frac{2z_0}{c}\right)\right) & \mathrm{sinc}\left(2W\left(t_0-\frac{2z_1}{c}\right)\right) & \cdots & \mathrm{sinc}\left(2W\left(t_0-\frac{2z_{M-1}}{c}\right)\right) \\ \mathrm{sinc}\left(2W\left(t_1-\frac{2z_0}{c}\right)\right) & \mathrm{sinc}\left(2W\left(t_1-\frac{2z_1}{c}\right)\right) & \cdots & \mathrm{sinc}\left(2W\left(t_1-\frac{2z_{M-1}}{c}\right)\right) \\ \vdots & \vdots & \ddots & \vdots \\ \mathrm{sinc}\left(2W\left(t_{N-1}-\frac{2z_0}{c}\right)\right) & \mathrm{sinc}\left(2W\left(t_{N-1}-\frac{2z_1}{c}\right)\right) & \cdots & \mathrm{sinc}\left(2W\left(t_{N-1}-\frac{2z_{M-1}}{c}\right)\right) \end{bmatrix} \begin{bmatrix} A_0 \\ A_1 \\ \vdots \\ A_{M-1} \end{bmatrix}, \tag{16}$$

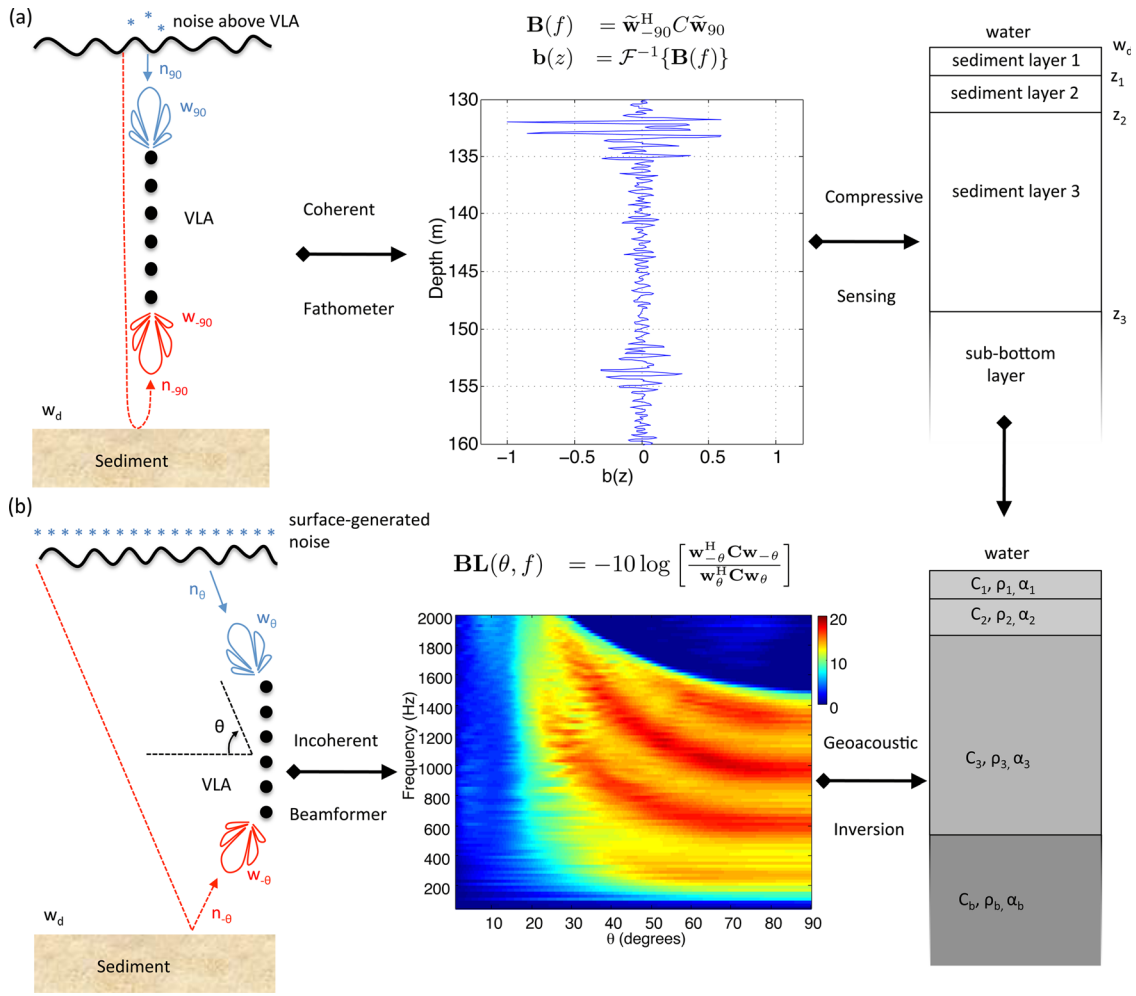

FIG. 1. (Color online) Description of the method: (a) Coherent fathometer processing by cross-correlating the upward and downward propagating surface-generated noise. The number of interfaces and their locations are estimated using compressive sensing. (b) Incoherent bottom loss estimation using beamforming. The bottom loss is obtained by dividing the bottom-reflected upward propagating noise by the downward propagating noise. This estimates bottom loss as a function of frequency and angle. Coupled with the layering information obtained from the fathometer results, a final geoacoustic inversion is performed.

where N is the number of measurements and $\mathbf{b}(\mathbf{x})$ is the forward model data vector corresponding to the fathometer output at $t = t_0,\ldots,t_{N-1}$. This selection of $\mathbf{x}$ allows for the representation of the fathometer output as a linear function of $\mathbf{x}$ with a matrix of sinc functions $\mathbf{S}$.

Sediment layer transitions occur only at a few depths. Most of the entries of $\mathbf{x}$ are zero with only K non-zero entries with $K \ll N < M$. In this case, $\mathbf{x}$ is K-sparse and the passive fathometer inversion can be cast as a sparse recovery problem and be solved using CS techniques.[3] Here, the convex optimization package CVX (Ref. 32) is used for CS fathometer inversions.

Unlike conventional CS problems where the matrix $\mathbf{S}$ is composed of random entries,[3] $\mathbf{S}$ here is a deterministic matrix composed of sinc functions with correlated entries. It has been shown that many deterministic matrices also work in CS, especially with highly spare parameter vectors.[28] With a sparsity $K/M < 5\%$, the CS fathometry works well with its deterministic sinc matrix.

B. Incoherent processing: Bottom loss calculation

Information about the ocean environment can be extracted incoherently using ambient noise.[2,22,33] Unlike the passive fathometer, the array is steered from broadside to end-fire estimating the plane wave power reflection coefficient R at each angle. The beamformer outputs are used incoherently by dividing the upward propagating noise level by the corresponding downward propagating noise level to estimate the plane wave power reflection coefficient R as a function of frequency and angle.[2]

MVDR beamforming has been shown[34] to result in errors for bottom loss calculations. Hence, a conventional beamformer is used here. The noise power level coming from θ is estimated as

$$N_\theta(f) = \mathbf{w}_\theta^{\mathrm{H}} \widehat{\mathbf{C}} \mathbf{w}_\theta. \tag{17}$$

The power reflection coefficient and bottom loss can be calculated as

$$\widehat{\mathbf{R}}^{\mathrm{obs}}(\theta,f) = \frac{N_{-\theta}(f)}{N_\theta(f)} = \frac{\mathbf{w}_{-\theta}^{\mathrm{H}} \widehat{\mathbf{C}} \mathbf{w}_{-\theta}}{\mathbf{w}_\theta^{\mathrm{H}} \widehat{\mathbf{C}} \mathbf{w}_\theta}, \tag{18}$$

$$\widehat{\mathbf{BL}}^{\mathrm{obs}}(\theta,f) = -10\log\widehat{\mathbf{R}} \quad 0^{\mathrm{o}} < \theta < 90^{\mathrm{o}}. \tag{19}$$

Note that Eq. (18) is an approximation to the true reflection coefficient. Since conventional beamforming is used to

obtain the upward and downward-propagating noise levels, Eq. (17) introduces some artifacts that result in the "smearing" of **R.**

The ideal $\mathbf{BL}(\theta, f)$ for a simple two-layer seafloor and isovelocity water column SSP is plotted as a function of frequency and angle in Fig. 2(a). For the same environment, the bottom loss $\widehat{\mathbf{BL}}^{\text{obs}}(\theta, f)$ estimated using beamforming under different "signal" to "noise" ratio (SNR) conditions is shown in Figs. 2(b)–2(d).

Low frequencies and/or a short array aperture lead to a broadening of the beam pattern, which in turn results in poor angle resolution. When the array is steered broadside at small θ, both bottom-reflected and surface-generated noise enters through the wide main lobe resulting in $\widehat{\mathbf{R}} = 1$. Hence $\widehat{\mathbf{BL}}^{\text{obs}}(\theta, f)$ at low frequencies and angles in Fig. 2(b) is closer to 0 dB than the true $\mathbf{BL}(\theta, f)$ given in Fig. 2(a).

If the inter-element spacing d is larger than half the wavelength at frequency f, grating lobes becomes an issue, resulting in a loss of the true value of $\mathbf{BL}(\theta, f)$; see the high frequency and angle region in Figs. 2(b)–2(d).

Surface generated noise constitutes the signal being processed. Bottom loss estimation depends on the ratio of noise coming from two different directions. Hence, all other noise sources including the receiver electronic self-noise set a noise-floor for the upward and downward propagating noise estimates.[25] This noise-floor effect is particularly pronounced when the surface-generated noise strength is low (calm sea) and at frequency-angle combinations where the bottom loss is high. At angles and frequencies with very high bottom loss, the bottom-reflected noise propagating upwards drops below the noise floor level. Figures 2(b)–2(d) corresponding to infinite, high, and low SNR show this effect with decreasing surface generated noise strength. Note that the high bottom loss regions in Fig. 2(b) are affected the worst in Fig. 2(d).

The first forward model candidate is OASN (Ref. 35) that simulates a range-independent surface sheet of noise and

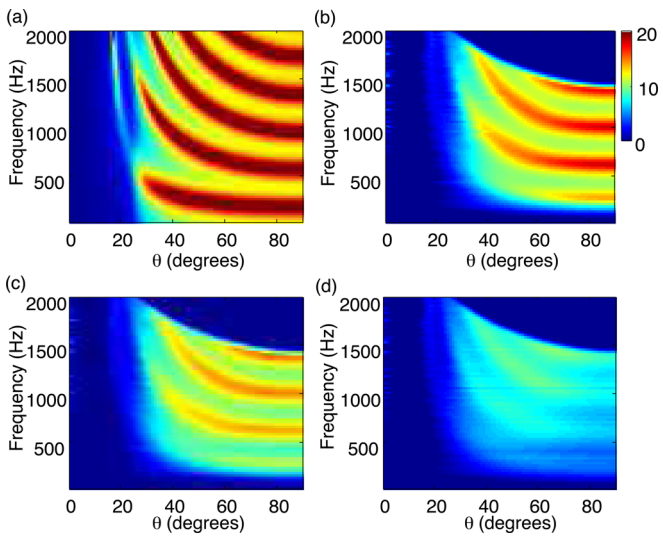

FIG. 2. (Color online) Bottom loss calculations for a simple two-layer seafloor and isovelocity water column SSP: (a) Ideal reflection loss obtained from OASR. Bottom loss obtained by OASN and beamforming with (b) infinite SNR, (c) high SNR (20 dB), and (d) low SNR (2 dB).

produces the noise CSDM $\mathbf{C}(\mathbf{x}_{\text{BL}})$ for a given environment $\mathbf{x}_{\text{BL}}$. Then, conventional beamforming is used to estimate upward and downward propagating noise power vs θ and $\widehat{\mathbf{BL}}(\mathbf{x}_{\text{BL}},\theta, f)$ is computed at each frequency and angle. The OASN method can be computationally demanding so an approximate method that is based on the ideal power reflection coefficient **R** obtained via OASR has been developed.[25,36]

The noise-floor effects mentioned earlier have been modeled[25] by incorporating a SNR. The SNR is defined as the ratio of the surface generated noise to the electronic self-noise power. Assuming a spatially white self-noise with variance $\sigma^2(f)$ across the array at frequency f and taking into account the array gain L, the bottom loss forward model becomes

$$\widehat{\mathbf{BL}}(\mathbf{x}_{\text{BL}}, \theta, f) = -10 \log \frac{\mathbf{w}_{-\theta}^{\text{H}} \mathbf{C}(\mathbf{x}_{\text{BL}}) \mathbf{w}_{-\theta} + \sigma^2/L}{\mathbf{w}_{\theta}^{\text{H}} \mathbf{C}(\mathbf{x}_{\text{BL}}) \mathbf{w}_{\theta} + \sigma^2/L}. \quad (20)$$

This forward model can estimate the observed bottom loss if the self-noise level $\sigma^2(f)$ is known at each frequency that is used in the inversion.[25] One solution involves incorporating the noise at each frequency as an unknown parameter in $\mathbf{x}_{\text{BL}}$. This gives the ability to characterize accurately the noise-floor effects but also results in an increased dimension of $\mathbf{x}_{\text{BL}}$. In order to prevent the number of unknown parameters from growing too large, only a small number of frequencies can be used in the inversion. This corresponds to using only a handful of horizontal slices of the information available in Fig. 2(b).

Here we adopt a method that estimates the beamformer output SNR from the observed data. The main assumption is that for most of the frequencies used in the inversion, there is an angle at which the bottom loss is large enough that the beamformer output in the numerator of Eq. (20) is dominated by the self-noise term. This allows us to define the minimum beamformer output across all negative angles (bottom-reflected, upward propagating) for each frequency as the self-noise level at that frequency. The average surface-generated noise (signal in this case) level at the beamformer output is estimated by averaging the beam- former output at positive angles (surface-generated, downward propagating). This gives a beamformer output $\widehat{\text{SNR}}$:

$$\widehat{\text{SNR}}(f) = \frac{\frac{1}{n_\theta} \sum_{\theta=\theta_0}^{90^\circ} \mathbf{w}_{\theta}^{\text{H}} \mathbf{C} \mathbf{w}_{\theta}}{\min\limits_{\theta_0 \le \theta \le 90^\circ} \mathbf{w}_{-\theta}^{\text{H}} \mathbf{C} \mathbf{w}_{-\theta}}, \quad (21)$$

where n_θ is the number of beam angles used to estimate the surface-generated noise and angles less than θ_0 are not used in the inversion.

An advantage of using $\widehat{\text{SNR}}$ values estimated from data is that the unknown parameter space is kept small. In addition, since the number of interfaces and layer depths are passed to the bottom loss inversion algorithm from the CS fathometer inversion, the inversion dimension can be kept significantly smaller than comparable methods and provides a fast inversion. As a result, OASN can be used here without having to resort to any approximate methods. Another

advantage is the ability to include a large number of frequencies in the inversion without changing the size of $\mathbf{x}_{\mathrm{BL}}$.

The downside of this approach is that the true self-noise level is less than the minimum of the beamformer output at each frequency (except when the bottom loss is very large), resulting in a $\widehat{\mathrm{SNR}}$ less than its true value. As the $\widehat{\mathrm{SNR}}$ estimated using Eq. (21) decreases, the error in the self-noise power estimation increases. A possible remedy for this problem is using only the frequencies that have high $\widehat{\mathrm{SNR}}$.

Finally, a simple ℓ_2-norm cost function is defined to optimize over the desired range of angles $\theta \in \Theta$ and frequencies $f \in F$:

$$\Phi(\mathbf{x}_{\mathrm{BL}}) = \sum_{\theta\in\Theta}\sum_{f\in F} ||\widehat{\mathbf{BL}}^{\mathrm{obs}}(\theta,f) - \widehat{\mathbf{BL}}(\mathbf{x}_{\mathrm{BL}},\theta,f)||_2, \tag{22}$$

where $\widehat{\mathbf{BL}}$ is calculated at $\mathbf{x}_{\mathrm{BL}}$ using Eq. (20) by adding a self-noise term σ^2 so that the SNR will match the $\widehat{\mathrm{SNR}}$ obtained in Eq. (21). Since the BL estimate uses θ less than 90°, a larger region around the vertical array will affect the results than with the passive fathometer.

C. Ambient noise inversion algorithm

The coherent fathometer inversion in Sec. III A and incoherent bottom loss inversion in Sec. III B are used together here in a two-step approach. First the number of bottom layers and depths are estimated. Then these are used to constrain a more complete seafloor geoacoustic inversion. The flow of calculations are as follows:

(1) A compressive passive fathometer inversion is performed by constructing Eq. (16). This algorithm assumes a K-sparse amplitude vector at M-depths with N measurements corresponding to the fathometer time series. A sparse estimate $\hat{\mathbf{x}}$ is obtained using CVX for the desired level of λ (larger λ means more compression, less interfaces).

(2) There are only K non-zero elements in $\hat{\mathbf{x}}$ whose depth values correspond to the water depth and sediment layer interface depths. Since the sinc basis function is an approximation, there will be some residual error between the true fathometer output and the sinc model at each layer interface. The inversion algorithm will need one or more closely-spaced apparent layers to fully represent the measured waveform at the layer interface, see Sec. III A. Thus, there are only K_e effective interfaces out of K reflectors. As long as a sediment layer is not very thin, it is straightforward to separate one closely-spaced set of apparent reflectors from another and determine K_e.

(3) As a result of the CS inversion, the bottom loss inversion starts with prior knowledge of the TWT estimates $\widehat{t_i} = 2\widehat{z_i}/c$ with $i = 0,\ldots,K_e-1$, which enables estimation of the water depth, the number of layer interfaces, and sediment thicknesses. Sediment layer thicknesses h_i only can be calculated during the bottom loss inversion since sediment layer sound speed c_i is needed in addition to the TWT t_i. It is possible to use the CS estimates $\widehat{t_i}$ and only invert for c_i in the BL inversion; however, we chose to incorporate the t_i as unknown parameters with tight priors around the CS estimates $\widehat{t_i}$.

(4) The full geoacoustic parameter vector for the BL inversion is given by (see Fig. 1)

$$\mathbf{x}_{\mathrm{BL}} = \left[\mathbf{h}^{\mathrm{T}} c_1\ \rho_1\ \alpha_1 \cdots c_{K_e}\rho_{K_e}\alpha_{K_e}\right]^{\mathrm{T}}, \tag{23}$$

$$\mathbf{h} = \begin{bmatrix} w_d \\ h_1 \\ h_2 \\ \vdots \\ h_{K_e-1} \end{bmatrix} = \begin{bmatrix} \frac{1}{2}c_w t_0 + z_{\mathrm{ref}} \\ \frac{1}{2}c_1(t_1 - t_0) \\ \frac{1}{2}c_2(t_2 - t_1) \\ \vdots \\ \frac{1}{2}c_{K_e-1}(tK_{e-1} - tK_{e-2}) \end{bmatrix}, \tag{24}$$

where w_d is the water depth, the K_eth layer corresponds to the sub-bottom layer, c_w is the average water column sound speed between the array and water-sediment interface, and z_{ref} is the depth of the reference array element. For each layer interface $i = 0,\ldots,K_e-1$, the maximum and minimum values obtained from the ith closely-spaced set of CS layer reflector estimates are set as upper and lower limits for t_i: $[\min(\widehat{t_i}), \max(\widehat{t_i})]$.

(5) The bottom loss inversion here is performed using GA. More advanced global inversion algorithms or Bayesian methods also can be used to infer uncertainty. The ability to use prior CS layering information reduces significantly the search space, resulting in consistent sediment sound speeds, attenuation, and density estimates. Here the CS inversion at each time is treated independently as the array drifts. However, since the bottom reflectors are continuous a sequential sparse sampling approach also could be applied.[37]

IV. BOUNDARY 2003 DRIFTING ARRAY DATA

The ambient noise data was collected by a drifting array in the NURC Boundary 2003 experiment.[1,17,19,20] The array consisted of 32 hydrophones with 0.18 m spacing (5.58 m total aperture) and a sampling rate of $f_s = 12$ kHz. The array drifted at 70 to 80 m depth with an average reference hydrophone depth of 73.5 m. The drifting array data was collected from July 22, 2003, 14:21 UTC (36.429° N, 14.785° E) to July 23, 2003, 03:28 UTC (36.414° N, 14.776° E). There was only one conductivity temperature depth (CTD) and one expendable bathythermograph (XBT) measurement recorded during this time (Fig. 3). However, the water column SSP during the experiment was fairly stable with the sound speed at the surface, array depth, and bottom measured as 1543, 1512, and 1512 m/s, respectively. The array drifted mostly parallel to the 130 m isobath so water depth along the path is relatively constant with only a marginal increase in depth over the data collection period.

A. Compressive fathometer inversion

MVDR passive fathometer processing was carried out over the 50 to 4000 Hz band ($W = 3950$ Hz). Each

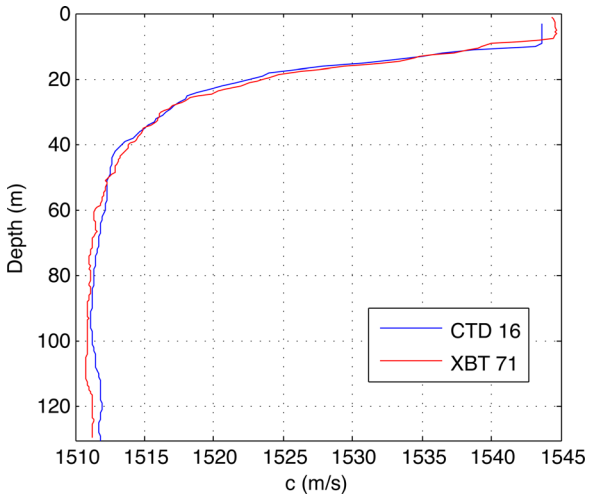

FIG. 3. (Color online) SSPs measured during the drifting portion of the Boundary 2003 experiment (July 22–23, 2003).

covariance matrix $\widehat{\mathrm{C}}$ was computed from 90 s data using 16 000 fast Fourier transform (FFT) bins with 50% overlap, corresponding to ∼120 snapshots. For the CS inversion, Eq. (16) is formed using $\Delta z = 2$ cm from 125 to 165 m, giving $M = 2000$. The fathometer output is obtained at $N = 640$ points (TWTs) at the acoustic data sampling rate f_s. Depending on the desired level of detail [controlled by λ in Eq. (7)], the number of non-zero entries, K, fluctuates between 3 and 80. As an example, $K = 20$ results in a K-sparse $\mathbf{x}$ where 99% of the entries are zero.

The drifting VLA track also was surveyed using a Uniboom active seismic system. Since the MVDR fathometer results have been shown to outperform significantly those produced by the conventional fathometer,[19] the MVDR fathometer is used here. The MVDR fathometer output is first compared with the Uniboom survey results in Fig. 4. To compare various reflector depth inversion methods, the area marked by the rectangle in Fig. 4(b) is explored in detail.

First, a GA inversion is performed using Eq. (14) to describe a fixed six-interface (including sediment-water interface) environment. The MVDR fathometer GA inversions are given in Fig. 5(b) where the background image is

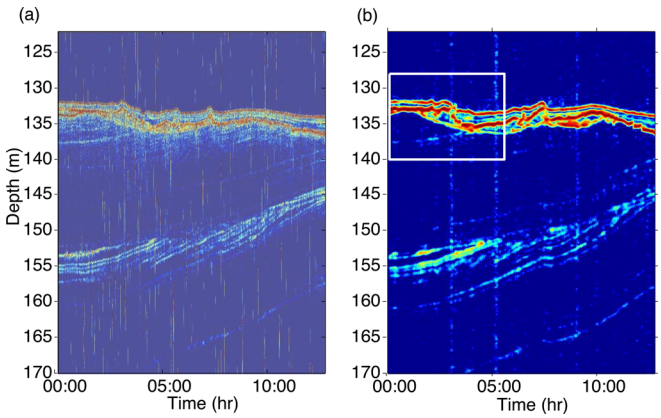

FIG. 4. (Color online) (a) Uniboom active seismic survey result along approximately the same track as the drifting VLA and (b) MVDR fathometer outputs. Rectangle shows the area explored in detail in Fig. 5. TWT is converted into depth using $c = 1500$ m/s.

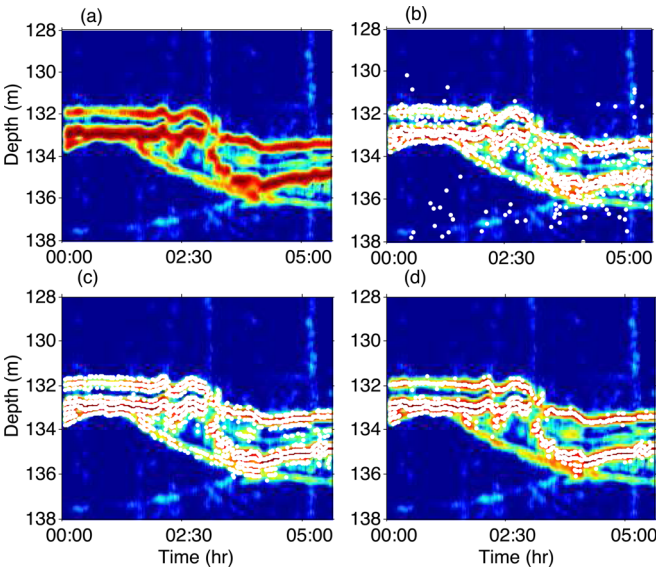

FIG. 5. (Color online) Fathometer inversion results: (a) MVDR fathometer output, (b) GA inversion results assuming a known number of interfaces ($K = 6$), CS inversion results for (c) $\lambda = 0.3$ and (d) $\lambda = 0.55$. TWT is converted into depth using $c = 1500$ m/s.

taken from the fathometer results in Fig. 5(a). Figures 5(c) and 5(d) gives the results for compressive MVDR inversion for two λ values. The outputs in both follow the tracks with minimal error. However, the number of interfaces are different in the two cases. The first case with $\lambda = 0.3$ enforces less

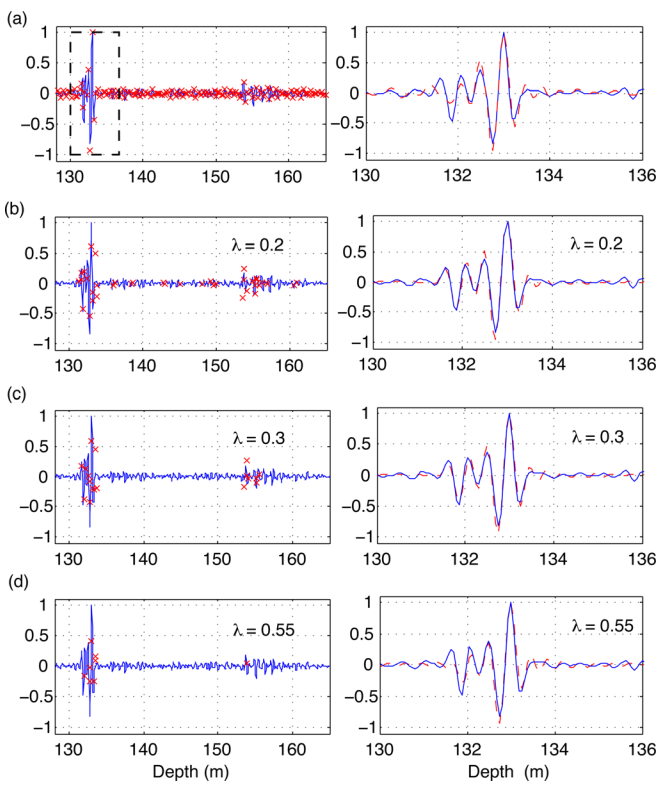

FIG. 6. (Color online) Four inversion results (×) using the MVDR fathometer output at 00:00 h with TWT converted into depth using $c = 1500$ m/s: (a) ℓ_2-norm inversion with regularization, and CS inversions with (b) $\lambda = 0.2$, (c) $\lambda = 0.3$, and (d) $\lambda = 0.55$. The right column plots are zoomed [rectangle in (a)] sections of the time-series where $\mathbf{b}(\widehat{\mathbf{x}})$ (dashed line) is compared to the observed fathometer output (solid line).

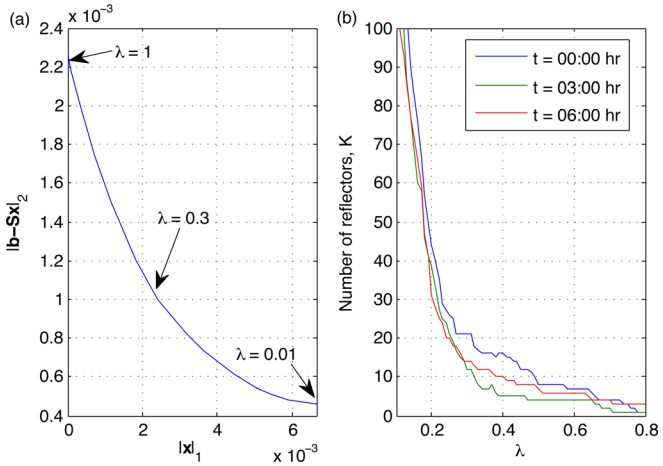

FIG. 7. (Color online) CS inversion analysis. (a) Relative contributions of the error terms $||b - \mathbf{Sx}||_2$ and $||\mathbf{x}||_1$ to the total cost function as a function of λ at $t = 00{:}00$ h. (b) Number of reflectors, K vs λ for $t = 00{:}00$, 03:00, 06:00 h.

compression. Hence more reflectors are allowed. In contrast, with a high value of λ (0.55), only the strongest reflectors are detected. The reason for this is the heavy penalty in the cost function as the number of reflectors increases. There is no unique answer regarding which one is better. The small λ case gives a more detailed set of reflectors. A coarser representation such as in Fig. 5(d) might be preferable for geoacoustic inversion purposes.

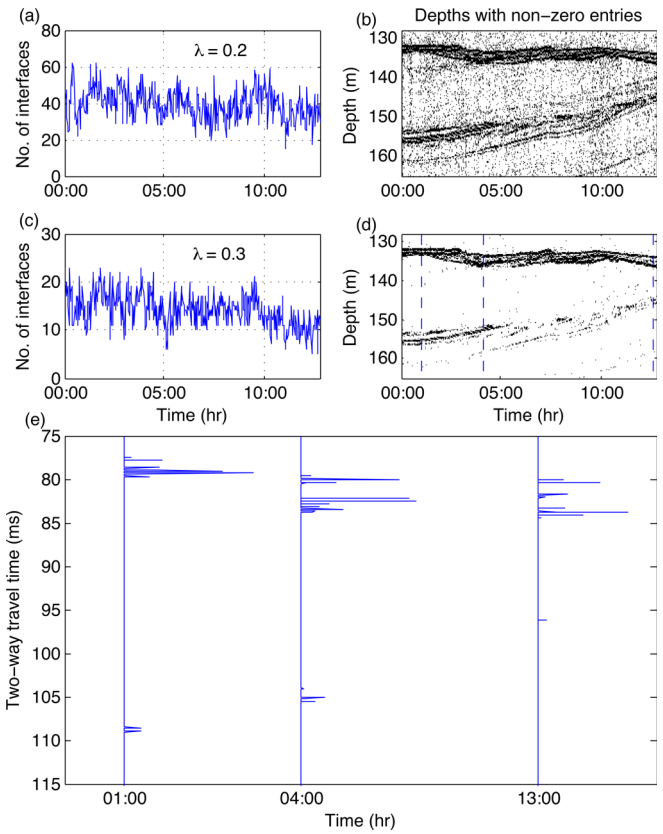

FIG. 8. (Color online) Fathometer inversion results: (a) Number of interfaces and (b) depths with non-zero entries (from TWT with $c = 1500$ m/s) for $\lambda = 0.2$. (c) and (d) are the results for $\lambda = 0.3$. (e) CS inversion results at three times (vertical cuts at 01:00, 04:00, and 13:00 h) that are used in the bottom loss inversion ($\lambda = 0.3$).

TABLE I. CS inversion results with $\lambda = 0.3$: Upper (U) and lower (L) boundaries of TWTs and corresponding CS inversion geoacoustic parameter estimates $\widehat{x}$ ($\widehat{w}_d$ and layer interface depths) assuming $c = 1500$ m/s.

TWT/$\widehat{x}$		01:00 h	04:00 h	13:00 h
$\widehat{t}_0(\widehat{w}_d^{cs})$	L	77.6 (131.7)	79.6 (133.2)	80.1 (133.6)
ms (m)	U	78.0 (132.0)	80.4 (133.8)	80.4 (133.8)
$\widehat{t}_1(\widehat{z}_1^{cs})$	L	78.9 (132.7)	81.9 (134.9)	81.7 (134.8)
ms (m)	U	79.5 (133.1)	83.3 (136.0)	82.1 (135.1)
$\widehat{t}_2(\widehat{z}_2^{cs})$	L	—	—	83.3 (136.0)
ms (m)	U	—	—	84.4 (136.8)
$\widehat{t}_3(\widehat{z}_b^{cs})$	L	108.5 (154.9)	105.2 (152.4)	95.9 (145.4)
ms (m)	U	108.9 (155.2)	105.7 (152.8)	96.3 (145.7)

Sometimes more than one reflector is needed in Figs. 5(b)–5(d) to characterize a layer interface. This is due in part to the mismatch between the fathometer output and the sinc wavelet in Eq. (13) as discussed in Secs. III A–III C. Thus, both GA and CS methods might require two or more closely-spaced sinc wavelets to match the fathometer output at each interface. Therefore a K-sparse CS inversion will have $K_e \leq K$ interfaces.

The difference between K and K_e can be reduced by increasing λ; however, a large λ runs the risk of missing weaker reflectors altogether.

The CS inversion results also can be compared with ℓ_2-norm inversions with regularization using Eq. (4) at 00:00 h. The pseudo-inverse solution in Fig. 6(a) yields a noisy reflection coefficient sequence with clusters of larger amplitudes at 131 to 135 m (water-sediment interface and the top sediment layer) and 153 and 157 m (a secondary series of interfaces). The synthetic fathometer output using the pseudo-inverse estimated environment matches well the measured fathometer response except for the small mismatch around 132 m, see Fig. 6(a). Three CS inversion results with increased sparseness are given in Figs. 6(b)–6(d). The results with $\lambda = 0.2$ show many reflectors with small but non-zero amplitudes, $\lambda = 0.3$ focuses well on the distinct interface regions with no reflectors in between, and finally $\lambda = 0.55$ mostly misses the reflectors at 150 to 160 m entirely and only does a good job of estimating the reflectors around 130 to 135 m. The synthetic fathometer outputs for all three values of λ give a better match to the fathometer response than does the pseudo-inverse method, demonstrating the advantages of using CS over classical ℓ_2-norm based inversions for the fathometer inversion problem.

TABLE II. Bottom loss inversion lower and upper bounds for the ith interface and water depth (z_a is the array depth).

	Lower	Upper
w_d (m)	$z_a + \frac{cw}{2}\min(\widehat{t}_0)$	$z_a + \frac{cw}{2}\max(\widehat{t}_0)$
h_i (m)	$\frac{c_i}{2}\min(\widehat{t}_i - \widehat{t}_{i-1})$	$\frac{c_i}{2}\max(\widehat{t}_i - \widehat{t}_{i-1})$
c_1 (m/s)	1450	1600
c_2 (m/s)	1450	1750
c_3 (m/s)	1450	1750
c_b (m/s)	1600	1900
ρ_i (g/cm^3)	1	2.5
α_i (dB/λ)	0	2

TABLE III. Bottom loss inversion results: Means and standard deviations of the geoacoustic parameters.

	w_d	h_1	h_2	h_3	c_1	c_2	c_3	c_b
	(m)				(m/s)			
1 h	133.4 ± 0.1	1.0 ± 0.2	—	25.2 ± 0.5	1477 ± 24	—	1705 ± 27	1730 ± 47
4 h	135.1 ± 0.2	2.3 ± 0.4	—	19.7 ± 0.6	1467 ± 18	—	1715 ± 25	1742 ± 41
13 h	134.8 ± 0.1	1.3 ± 0.1	1.2 ± 0.3	10.7 ± 0.4	1471 ± 23	1515 ± 45	1701 ± 37	1761 ± 39
	ρ_1	ρ_2	ρ_3	ρ_b	α_1	α_2	α_3	α_b
	(g/cm^3)				(dB/λ)			
1 h	1.3 ± 0.1	—	1.5 ± 0.1	2.1 ± 0.3	0.2 ± 0.1	—	0.5 ± 0.3	0.6 ± 0.3
4 h	1.3 ± 0.1	—	1.5 ± 0.1	1.9 ± 0.3	0.1 ± 0.1	—	0.2 ± 0.1	0.6 ± 0.4
13 h	1.4 ± 0.1	1.6 ± 0.1	1.7 ± 0.1	2.0 ± 0.2	0.3 ± 0.2	0.1 ± 0.1	0.1 ± 0.1	0.3 ± 0.3

In order to explore the effect of λ on the CS inversion, the drifting array data have been inverted using CS with varying values of λ. Figure 7(a) shows the relative contributions of the terms forming the objective function in Eq. (7). For large λ, the objective function is heavily skewed toward sparseness. For this case, $\lambda \geq 1$ forces perfect sparseness $||\widehat{\mathbf{x}}||_1 \rightarrow 0$, effectively ignoring the data. For $\lambda \leq 0.01$, $||\widehat{\mathbf{x}}||_1 \ll ||\mathbf{b} - \mathbf{S}\widehat{\mathbf{x}}||_2$ and the CS inversion becomes a standard ℓ_2-norm inversion. The lowest value of the cost function in Eq. (7) is obtained at around $\lambda = 0.3$. The number of reflectors K needed as λ increases is provided in Fig. 7(b). Initially, K decreases rapidly as λ increases, then stabilizes before it drops further as $\lambda > 0.65$. The middle region with $\lambda = 0.25$–0.5 yields CS results with a modest number of reflectors while at the same time having a small cost function.

The CS results over the entire data are given in Fig. 8. The data is inverted at 90 s intervals as the array drifts. The evolving number of reflectors with time are given in Figs. 8(a) and 8(c) for two λ values. The $\lambda = 0.2$ case gives K between 18 and 61, whereas K initially is around 20 for $\lambda = 0.3$, decreasing to 10 as the deeper reflections get weaker. Figures 8(b) and 8(d) mark the non-zero entries in the depth vector (1 if a reflector exists at that depth and 0 for no reflector, not reflection amplitude). Most interfaces are represented by two or more sinc wavelets, up to tens of centimeters apart. The three times shown in Fig. 8(d) are displayed in Fig. 8(e). The CS inversion results in $K = 12$, 16, and 9, respectively. Since some reflectors have very small reflection amplitudes, fewer reflectors are observed in Fig. 8(e) than in Fig. 8(d). Assigning the closely spaced sincs to a single sediment layer interface results in $K_e = 3$, 3, and 4, respectively. For the entire track K_e ranges between 3 and 7. The lower and upper TWT/depth values for each of these K_e interfaces will form the prior for the bottom loss inversion, see Table I.

B. Incoherent bottom loss inversion

The upper and lower bounds for the geoacoustic parameters estimated in the bottom loss inversion are given in Table II. Due to the small array aperture, the beam was large at low frequencies. The element spacing of 0.18 m corresponds to a half-wavelength at $f = 4167$ Hz. The frequency band 300 to 4000 Hz is used in the bottom loss calculations with 100 Hz spacing. Also, due to the large main lobe width, the power reflection coefficient $\widehat{\mathbf{R}}$ cannot accurately be estimated by Eq. (18) at small θ as described in Sec. III B. Hence, the bottom loss is calculated for $\theta = 25°$ to $90°$ with $\Delta\theta = 1°$.

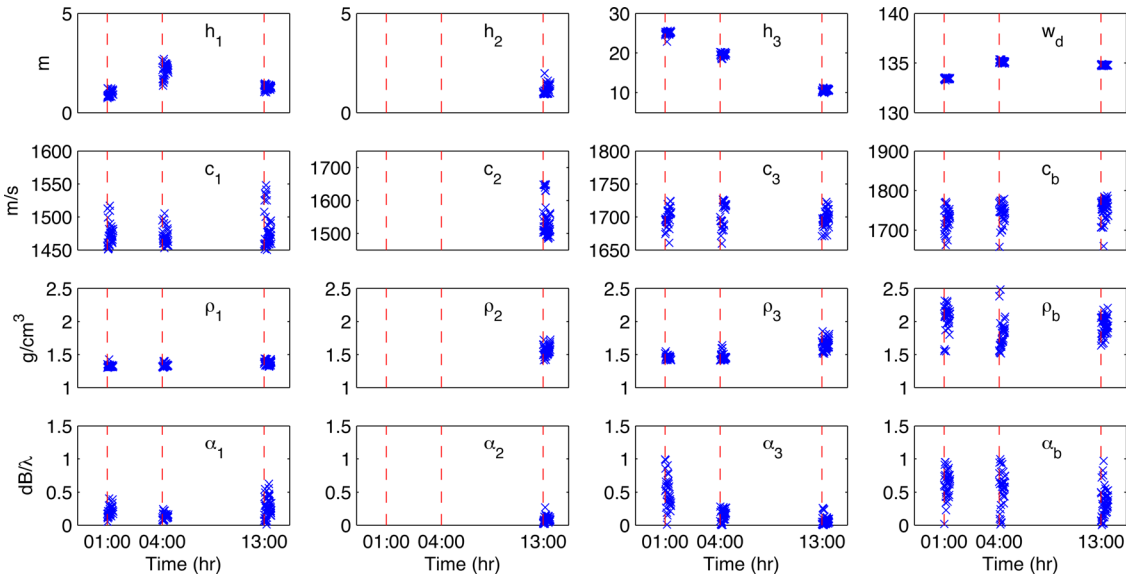

FIG. 9. (Color online) Bottom loss inversion results: Scatter plots for independent GA inversions at three times along the track.

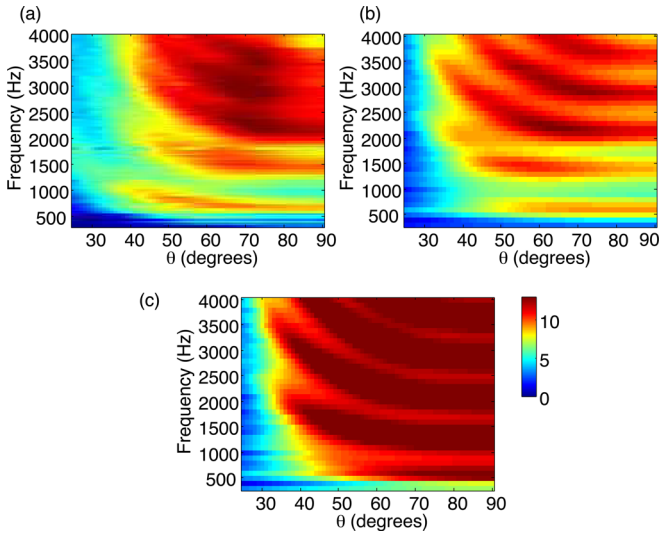

FIG. 10. (Color online) Fathometer inversion results: Bottom loss as a function of frequency and angle obtained from (a) observed data, (b) forward model evaluated at $\widehat{\mathbf{x}}_{\mathrm{BL}}$ with $\widehat{SNR}$ estimated from the data, and (c) forward model evaluated at $\widehat{\mathrm{x}}_{\mathrm{BL}}$ without self-noise.

The region where the data was collected lies on the Straits of Sicily (Malta Plateau), just to the west of the Ragusa Ridge and is well-documented[38,39] with a number of experiments (see Fig. 9 in Ref. 17). Unlike the Ragusa Ridge where the bottom has bare rock formations and no sediment, the basin is covered with high-porosity silty-clay sediment.[40] The closest area explored in previous studies is located just south of the Boundary 2003 drifting array location, named Site 1 data in Ref. 40. A set of core measurements (Fig. A-3 of Ref. 41 and Fig. 4 in Ref. 40) for this site shows a low sediment sound speed (1470 m/s) at the top of the first layer that increases to around 1500 m/s at 1 m, and density starting at 1.3 to 1.4 g/cm^3 at the water-sediment interface increasing gradually to ∼1750 m/s and ∼2 g/cm^3. A little north of the drifting array lies Site 4 with a homogeneous soft silty-clay[40] with a sound speed of 1500 m/s at the top of the sediment and a density of 1.5 g/cm^3. West of the drifting array location, the sediment parameters[42] given by Fig. 15 and Table VI in Ref. 43 show sound speed values greater than 1600 m/s at depths more than 6 m with a bottom sound speed at 1800 m/s.

The results of the bottom loss inversion are given in Table III. Following the CS inversion results in Fig. 8(e), the first two times (01:00 and 04:00 h) are represented by a three-layer sediment whereas the last time (13:00 h) has a fourth interface. Statistics for the parameter estimates are obtained by independently inverting data segments collected around the three cases. Each data segment close to the desired time is inverted by GA. The estimated environment obtained from each data segment is plotted in scatter plot form in Fig. 9 for all three cases. Along the track, the top 5 m can be represented by 1 to 4 layers as shown in Fig. 5. The first layer has a low sound speed around 1470 m/s supported by both core measurements and prior inversion results.[25,44–46] Similarly, the bottom sound speed values of ∼1740 m/s is in good agreement with Site 1 results.[40,44,45] The inversion results compare well with the Site 1 data[40] closest to the drifting array location. The sediment density starts at 1.3 to 14 g/cm^3 and the bottom density is ∼1.9 g/cm^3, again in agreement with previous work. The attenuation is poorly determined and has a large standard deviation similar to previous studies.[25,45] Some parameters such as c_2 have multiple possible solutions as expected from the typical nonlinear/non-Gaussian behavior of geoacoustic inversion results. In addition, sediment properties are harder to invert as depth increases.

The observed bottom loss in Fig. 10(a) compares well with the synthetic data in Fig. 10(b) obtained by Eq. (20) using the solution $\widehat{\mathbf{x}}_{\mathrm{BL}}$ at 01:00 h, with the OASN forward model $\widehat{SNR}$. The importance of self-noise can be observed by comparing Fig. 10(b) with the ideal bottom loss plot for $\widehat{\mathbf{x}}_{\mathrm{BL}}$ without self-noise in Fig. 10(c). Even though Figs. 10(b) and 10(c) belong to the same environment, Fig. 10(c) fits poorly with the data in Fig. 10(a).

V. CONCLUSIONS

A geoacoustic parameter estimation algorithm has been introduced that incorporates both coherent passive fathometry and incoherent passive bottom loss estimation. The sparse nature of some of the geoacoustic parameters such as water depth and sediment thicknesses was exploited by introducing a CS fathometer inversion algorithm as a first step. The CS algorithm incorporated a ℓ_1-norm term in the objective function in addition to the ℓ_2-norm error term. The results of the CS inversion were then used as priors in a bottom loss inversion.

The algorithm was demonstrated on the Boundary 2003 drifting array data. The number of layers were tracked by the CS algorithm. The water depth and layer thicknesses were inverted with small uncertainties and this facilitated the inversion of other bottom parameters such as sound speed, attenuation, and density.

ACKNOWLEDGMENTS

The authors would like to thank Peter Nielsen of NATO CMRE, La Spezia, Italy for providing the Boundary 2003 data. This work was supported by the Office of Naval Research, under Grant No. N00014-11-1-0320.

[1]M. Siderius, C. H. Harrison, and M. B. Porter, "A passive fathometer technique for imaging seabed layering using ambient noise," J. Acoust. Soc. Am. **120**, 1315–1323 (2006).
[2]C. H. Harrison and D. G. Simons, "Geoacoustic inversion of ambient noise: A simple method," J. Acoust. Soc. Am. **112**, 1377–1389 (2002).
[3]D. L. Donoho, "Compressed sensing," IEEE Trans. Inf. Theory **52**, 1289–1306 (2006).
[4]E. J. Candès, J. Romberg, and T. Tao, "Robust uncertainty principles: Exact signal reconstruction from highly incomplete frequency information," IEEE Trans. Inf. Theory **52**, 489–509 (2006).
[5]M. Lustig, D. Donoho, and J. M. Pauly, "Sparse MRI: The application of compressed sensing for rapid MR imaging," Magn. Reson. Med. **58**, 1182–1195 (2007).
[6]R. G. Baraniuk, E. Candes, M. Elad, and Y. Ma, "Applications of sparse representation and compressive sensing," Proc. IEEE **98**, 906–909 (2010).
[7]M. Elad, *Sparse and Redundant Representations* (Springer, New York, 2010), pp. 1–376.
[8]H. Yao, P. Gerstoft, P. M. Shearer, and C. F. Mecklenbräuker, "Compressive sensing of the Tohoku–Oki Mw 9.0 earthquake: Frequency-dependent rupture modes," Geophys. Res. Lett. **38**, L20310, doi:10.1029/2011GL049223 (2011).

[9]N. R. Chapman and I. Barrodale, "Deconvolution of marine seismic data using the ℓ_1 norm," Geophys. J. Int. **72**, 93–100 (1983).
[10]F. Fazel, M. Fazel, and M. Stojanovic, "Random access compressed sensing for energy- efficient underwater sensor networks," IEEE J. Sel. Areas Commun. **29**, 1660–1670 (2011).
[11]W. U. Bajwa, J. Haupt, A. M. Sayeed, and R. Nowak, "Compressed channel sensing: A new approach to estimating sparse multipath channels," Proc. IEEE **98**, 1058–1076 (2010).
[12]C. R. Berger, S. Zhou, J. C. Preisig, and P. Willett, "Sparse channel estimation for multicarrier underwater acoustic communication: From subspace methods to compressed sensing," IEEE Trans. Signal Process. **58**, 1708–1721 (2010).
[13]G. F. Edelmann and C. F. Gaumond, "Beamforming using compressive sensing," J Acoust. Soc. Am. **130**, EL232–EL237 (2011).
[14]W. Mantzel, J. Romberg, and K. Sabra, "Compressive matched-field processing," J. Acoust. Soc. Am. **132**, 90–102 (2012).
[15]D. Malioutov, M. Çetin, and A. S. Willsky, "A sparse signal reconstruction perspective for source localization with sensor arrays," IEEE Trans. Signal Process. **53**, 3010–3022 (2005).
[16]E. J. Candès and M. B. Wakin, "An introduction to compressive sampling," IEEE Signal Process. Mag. **25**, 21–30 (2008).
[17]C. H. Harrison and M. Siderius, "Bottom profiling by correlating beam-steered noise sequences," J. Acoust. Soc. Am. **123**, 1282–1296 (2008).
[18]P. Gerstoft, W. S. Hodgkiss, M. Siderius, C.-F. Huang, and C. H. Harrison, "Passive fathometer processing," J. Acoust. Soc. Am. **123**, 1297–1305 (2008).
[19]M. Siderius, H. Song, P. Gerstoft, W. S. Hodgkiss, P. Hursky, and C. Harrison, "Adaptive passive fathometer processing," J. Acoust. Soc. Am. **127**, 2193–2200 (2010).
[20]J. Traer, P. Gerstoft, and W. S. Hodgkiss, "Ocean bottom profiling with ambient noise: A model for the passive fathometer," J. Acoust. Soc. Am. **129**, 1825–1836 (2011).
[21]Z.-H. Michalopoulou, C. Yardim, and P. Gerstoft, "Particle filtering for passive fathometer tracking," J. Acoust. Soc. Am. **131**, EL74–EL80 (2012).
[22]C. H. Harrison, "Sub-bottom profiling using ocean ambient noise," J. Acoust. Soc. Am. **115**, 1505–1515 (2004).
[23]M. Siderius and C. Harrison, "High-frequency geoacoustic inversion of ambient noise data using short arrays," AIP Conf. Proc. **728**, 22–31 (2004).
[24]J. I. Arvelo, Jr., "Robustness and constraints of ambient noise inversion," J. Acoust. Soc. Am. **123**, 679–686 (2008).
[25]J. E. Quijano, S. E. Dosso, J. Dettmer, L. M. Zurk, M. Siderius, and C. H. Harrison, "Bayesian geoacoustic inversion using wind-driven ambient noise," J. Acoust. Soc. Am. **131**, 2658–2667 (2012).
[26]J. E. Quijano, S. E. Dosso, J. Dettmer, L. M. Zurk, and M. Siderius, "Trans-dimensional geoacoustic inversion of wind-driven ambient noise," J. Acoust. Soc. Am. **133**, EL47–EL53 (2012).
[27]R. G. Baraniuk, "Compressive sensing," IEEE Signal Process. Mag. **24**, 118–121 (2007).
[28]H. Monajemi, S. Jafarpour, M. Gavish, Stat 330/CME 362 Collaboration, and D. L. Donoho, "Deterministic matrices matching the compressed sensing phase transitions of Gaussian random matrices," Proc. Natl. Acad. Sci. U.S.A. **110**, 1181–1186 (2013).
[29]S. Boyd and L. Vandenberghe, *Convex Optimization* (Cambridge University Press, New York, 2004), pp. 1–701.
[30]W. A. Kuperman and F. Ingenito, "Spatial correlation of surface generated noise in a stratified ocean," J. Acoust. Soc. Am. **67**, 1988–1996 (1980).
[31]J. Traer and P. Gerstoft, "Coherent averaging of the passive fathometer response using short correlation time," J. Acoust. Soc. Am. **130**, 3633–3641 (2011).
[32]M. Grant, S. Boyd, and Y. Ye, CVX: MATLAB software for disciplined convex programming, http://cvxr.com/cvx (Last viewed October 1, 2013).
[33]N. M. Carbone, G. B. Deane, and M. J. Buckingham, "Estimating the compressional and shear wave speeds of a shallow water seabed from the vertical coherence of ambient noise in the water column," J. Acoust. Soc. Am. **103**, 801–813 (1998).
[34]L. Muzi, M. Siderius, J. Gebbie, and J. Paddock, "On the use of adaptive beam forming techniques for geoacoustic inversion of marine ambient noise," in *Proceedings of the IEEE OCEANS Conference* (Seattle, WA, 2010), pp. 1–6.
[35]H. Schmidt, OASES: Version 3.1, user guide and reference manual, http://acoustics.mit.edu/faculty/henrik/oases.html (Last viewed October 1, 2013).
[36]C. H. Harrison, "Formulas for ambient noise level and coherence," J. Acoust. Soc. Am. **99**, 2055–2066 (1996).
[37]C. F. Mecklenbrauker, P. Gerstoft, A. Panahi, and M. Viberg, "Sequential Bayesian sparse source reconstruction using array data," IEEE Trans. Signal Process. **61**, 6344–6354 (2013).
[38]C. W. Holland, "Mapping seabed variability: Rapid surveying of coastal regions," J. Acoust. Soc. Am. **119**, 1373–1387 (2006).
[39]C. W. Holland, P. L. Nielsen, J. Dettmer, and S. Dosso, "Resolving meso–scale seabed variability using reflection measurements from an autonomous underwater vehicle," J. Acoust. Soc. Am. **131**, 1066–1078 (2012).
[40]C. W. Holland, "Coupled scattering and reflection measurements in shallow water," IEEE J. Ocean. Eng. **27**, 454–470 (2002).
[41]C. W. Holland, R. C. Gauss, P. C. Hines, P. Nielsen, J. R. Preston, C. H. Harrison, D. D. Ellis, K. D. LePage, J. Osler, R. W. Nero, D. Hutt, and A. Turgut, "Boundary characterization experiment series overview," IEEE J. Ocean. Eng. **30**, 784–806 (2005).
[42]A. Turgut, "Inversion of bottom/sub-bottom statistical parameters from acoustic backscatter data," J. Acoust. Soc. Am. **102**, 833–852 (1997).
[43]J. R. Preston, D. D. Ellis, and R. C. Gauss, "Geoacoustic parameter extraction using reverberation data from the 2000 Boundary Characterization Experiment on the Malta Plateau," IEEE J. Ocean. Eng. **30**, 709–732 (2005).
[44]M. R. Fallat, P. L. Nielsen, S. E. Dosso, and M. Siderius, "Geoacoustic characterization of a range-dependent ocean environment using towed array data," IEEE J. Ocean. Eng. **30**, 198–206 (2005).
[45]J. Dettmer, S. E. Dosso, and C. W. Holland, "Model selection and Bayesian inference for high-resolution seabed reflection inversion," J. Acoust. Soc. Am. **125**, 706–716 (2009).
[46]P. L. Nielsen and C. Harrison, "Combined geoacoustic inversion of propagation and reverberation data," IEEE J. Ocean. Eng. **34**, 51–62 (2009).